Supplementary Information

D. J. G. Pearce, A. M. Miller, G. Rowlands and M. S. Turner

1 Methods

1.1 Numerical Simulations

Simulation of the hybrid projection model involves solving the equations of motion Eqs. 2 & 3 (main text) in both 2D and 3D.

For the 2D simulations each individual selects σ nearest visible neighbours; here we define a member of the swarm as visible if it is possible to draw an unbroken line of sight from the individual to any point of its neighbour. If there are fewer than σ visible neighbours for an individual it uses the orientation information from all visible neighbours, this has no major effect since this component of the velocity is normalised upon its inclusion in Eq. 3.

These were solved iteratively using an algorithm written in C++. The initial conditions for the N individuals were that they started with random positions in a square region of space of area N^2 (in units of the size of each individual squared) with randomly orientated velocities. So as to eliminate transients associated with these arbitrary initial conditions the swarms are allowed to pre-equilibrate. The pre-equilibration period was at least 25,000 time steps for simulations contributing to the phase planes, such as Fig. 2b,c, and for the simulations contributing to swarm scaling results, such as Fig. 2d, where the size of the swarm was sometimes much larger. The pre-equilibration period was always longer than the corresponding correlation time, as shown in Fig. 2f (except when $\phi_p = 0$, when the swarm anyway fragments and disperses to infinity).

Scaling results, as shown in Fig. 2d, were averaged over 50,000 timesteps. Phase planes, as shown in Fig. 2b,c,e,f and Fig. S16,S17, show results for 861 different locations in the parameter space, each being the average result of four simulations of 100,000 time steps at that particular combination of ϕ_p and ϕ_a.

The angular size presented to individual i by its neighbour j depends on the physical size

of the individual b and vector connecting them $\mathbf{r}_{ij}$. For the isotropic individuals considered in most of the article this is defined to be

$$\Delta\theta = 2\arctan\left(\frac{b}{2|\mathbf{r}_{ij}|}\right) \tag{1}$$

which approaches $\Delta\theta = b/|\mathbf{r}_{ij}|$ for $r \gg b$. For anisotropic individuals (Figs. S16,S17,S18 and Supp.Movs, S5-S9, only) the angular size of the j^{th} individual depends on the angle ζ_{ij} between its direction of motion, along $\mathbf{v}_j$, and the line of sight of the i^{th} individual to it, along $\mathbf{r}_{ij}$. If the aspect ratio is $a \geq 1$ and the long axis is orientated at an angle ψ to the direction of motion ($\psi = 0$ is long-and-thin, $\psi = \pi/2$ is short-and-fat) the angle subtended at $\mathbf{r}_i$ is defined to be

$$\Delta\theta = 2\arctan\left(\frac{\tilde{b}}{2|\mathbf{r}_{ij}|}\right) \tag{2}$$

with the apparent physical size in this orientation given by

$$\tilde{b} = b\left(\sin^2(\zeta+\psi) + a^2\cos^2(\zeta+\psi)\right)^{-1/2} \tag{3}$$

See Fig. S1. This reduces to $\tilde{b} = b$ when $a = 1$, as required,

There are several possible refinements that can be made to our model. The first of these would be to include short ranged repulsive interactions, although we expect this to have less effect in the low density (universal) regime of most interest to us here; this is explored in more detail later in the SI. Secondly one might relax the assumption that the velocity of the individuals is constant. It would also be possible to introduce a "blind angle" behind each individual from which it cannot obtain any information, similar to that employed in previous models [1]. This has little qualitative effect on the behaviour of the model, as shown in Supp.Movs. S8,S10,S9.

Another possible refinement would be to introduce an effective bird size in order to account for how individuals may assign continuity between dark regions. This could arise from a cognitive or visual blurring of each individual. Such blurring is quite natural, given that individuals rarely have very sharp edges (consider, for example, the feathers on a bird's wingtips). There

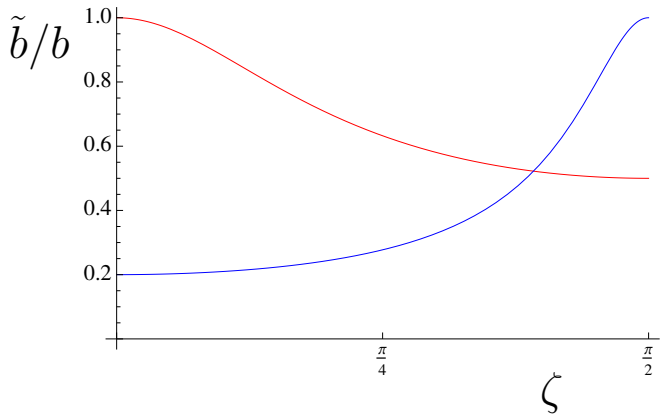

Figure 1:(SI) The apparent physical size $\tilde{b}$ of an anisotropic individual divided by its (maximum) length b. The individual's velocity is orientated at an angle ζ to the line of sight from the observer. The blue curve represents a long-and-thin individual, with long axis parallel to its velocity ($\psi = 0$) and aspect ratio $a = 5$. The red curve represents a short-and-fat individual, with long axis orientated at an angle $\psi = \pi/2$ to its velocity and aspect ratio $a = 2$.

is also the fact that vision has a limited angular resolution. In this case space could be thought of as being discretised into a number of angular "bins" and an observer must assign each bin as full or empty depending on whether or not it contains (at least) one bird. Here the physical bird size would naturally be replaced by the bin (blurring envelope) size. Given these issues it may be wise to regard the bird size in our model as not necessarily being identical to any (arbitrary) physical size. This refinement could explain the (rather small) numerical discrepancy between the quantitative value of the opacity seen in Fig. 2c,d (our model) and Fig. 3b,d,e (data). Another attractive feature of our model is its relative robustness to physical limitations on visual resolution, both temporal and spatial (angular).

1.1.1 3D implementation

The 3D simulations were produced using the same equations of motion as the 2D model and employed an algorithm written in C++. A minor difference to the 2D implementation is that visible neighbours were defined using a Delaunay triangulation. The Delaunay triangulation

leads to a natural conception of neighbours due to it being the dual graph to the Voronoi construction, in which all points nearer to a data point than any other data point belong to that data point's Voronoi cell, hence neighbours defined through the Voronoi construction are those that share edges between their Voronoi cells and are in some sense 'closer' than those cells that do not share Voronoi edges.

The initial conditions for the N individuals is that they were placed randomly in a cube with a target density of 0.01 individuals per unit cube (in units of the individual radii). A pre-equilibration period of 20,000 time steps and measuring period of 80,000 time steps with 5 repeats at each parameter value were used for the 3D scaling results shown in Fig 2d (main text). All other results shown in the main text are for 2D.

Individuals are treated as isotropic bodies that obscure a line of sight from any other individual that passes through it. This results in the projection of (dark) circular caps onto the view of other individuals, treated as a unit sphere; the interior of any of these caps represent directions where an individual is unable to trace a line of sight to infinity (the light sky). These caps can overlap, leading to a patterning of the surface of each spherical view into "dark" and "light", see Fig 2(SI). The spherical cap projected by an individual j onto i's view is defined by a solid angle given by $\Gamma = 2\pi\left(1 - \frac{R}{\sqrt{1+R^2}}\right)$, where $R = |\mathbf{r}_{ij}|$ is the distance between the individuals. Hence Γ defines the angular size of the projection in 3D. This is equivalent to an individual j being viewed as a disk of unit radius with its normal always pointing towards the focal individual i. The boundaries of the occluded regions on the surface of the i^{th} individual are then unions of arcs of circles in 3D, collectively the set of contours C_i. The projected input to the equation of motion [3] is the following generalisation of Eq [1] to 3D

$$\underline{\delta}_i = \frac{\int_{\{C_i\}} \hat{r} dl}{\int_{\{C_i\}} dl} \tag{4}$$

where each integral is over infinitesimal line elements dl that trace along the curve(s) C_i sepa-

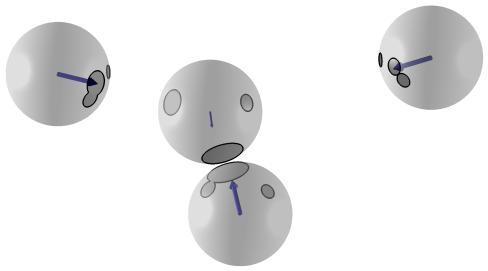

Figure 2:(SI) A sketch showing the projected views of a number of individuals in 3D analogous to that shown for 2D in Fig. 1(main text). The dark shaded regions represent the set of normal directions that correspond to lines of sight that intersect another individual. The vector $\underline{\delta}_i$ is displayed as a blue arrow for each individual i. It is given by Eq (4)SI and is essentially the average normal orientation of the boundary of the shaded region(s).

rating the "dark" and "light" regions on the surface of a unit sphere and $\hat{r}$ is the outward pointing unit vector at each point alone those curves.

1.2 Data Collection

Data on flocking starlings for Fig. 3a-d was collected from three separate sites during Autumn 2011, these were.

Strumpshaw, Norfolk, UK. GPS coordinates 52.35515, 1.28122. Date 24/09/2011 Time 17:56 (sunset -66 min).

Glastonbury, Somerset, UK. GPS coordinates 51.157052, -2.73676. Date 05/10/2011 Time 16:48 (sunset -110 min).

Brighton, East Sussex, UK. GPS coordinates50.816544, -0.136691. Date 10/10/2011 Time 18:10 (sunset -15 min).

Brighton, East Sussex, UK. GPS coordinates50.816544, -0.136691. Date 14/11/2011 Time 15:40 (sunset -7 min).

Brighton, East Sussex, UK. GPS coordinates50.816544, -0.136691. Date 14/11/2011 Time

16:10 (sunset -37 min).

A Panasonic HDC-SD600 camera was used to collect 1920 $\times$ 1080 video at 50 progressive frames per second. Frames from the video were analysed as individual images. The video sequences were discarded if they had any obvious obscuring of the flock, not all of the flock was visible, or the background was insufficiently monotone. Examples of collected footage is shown in Supp. Mov. S1, S2.

Images selected for analysis in Fig. 2e were *all those* returned on the first two pages of a Google image search for the phrase "starling flock" performed on July 27 2011. Images were discarded only if they didn't show a starling flock, had obviously been doctored in some manner, or were composite images. The image number shown on the horizontal axis of Fig. 3e corresponds to the ordered number in which that image was returned in the search. The first six of these images are fairly representative and are shown in Fig. S3. We believe that the lack of any subjective bias in the selection of these images of flocks, of various sizes under different light conditions, represents a rigorous test of our hypothesis that these flocks adopt a state of marginal opacity, see Fig. 3e.

1.3 Image Processing

We don't attempt direct identification of individual birds. Instead each image was converted to an 8-bit greyscale and connected regions of the flock were outlined by eye so as to exclude obvious foreground objects that weren't birds (if any) and regions of empty sky outside the flock (if any). For images that include more than one connected flock region the opacity was computed as the average of the distinct regions of the flock, weighted by their relative size in pixels. All pixels, with greyscale level g_i, $i \in [1, n]$ within the outline were considered to be within the flock. The greyscale distribution was analyzed to yield the average $\bar{g} = \frac{1}{n}\sum_{i=1}^{n} g_i$, maximum $g_{\max}$ and minimum $g_{\min}$ pixel greyscale levels (low numbers are darker). The opacity

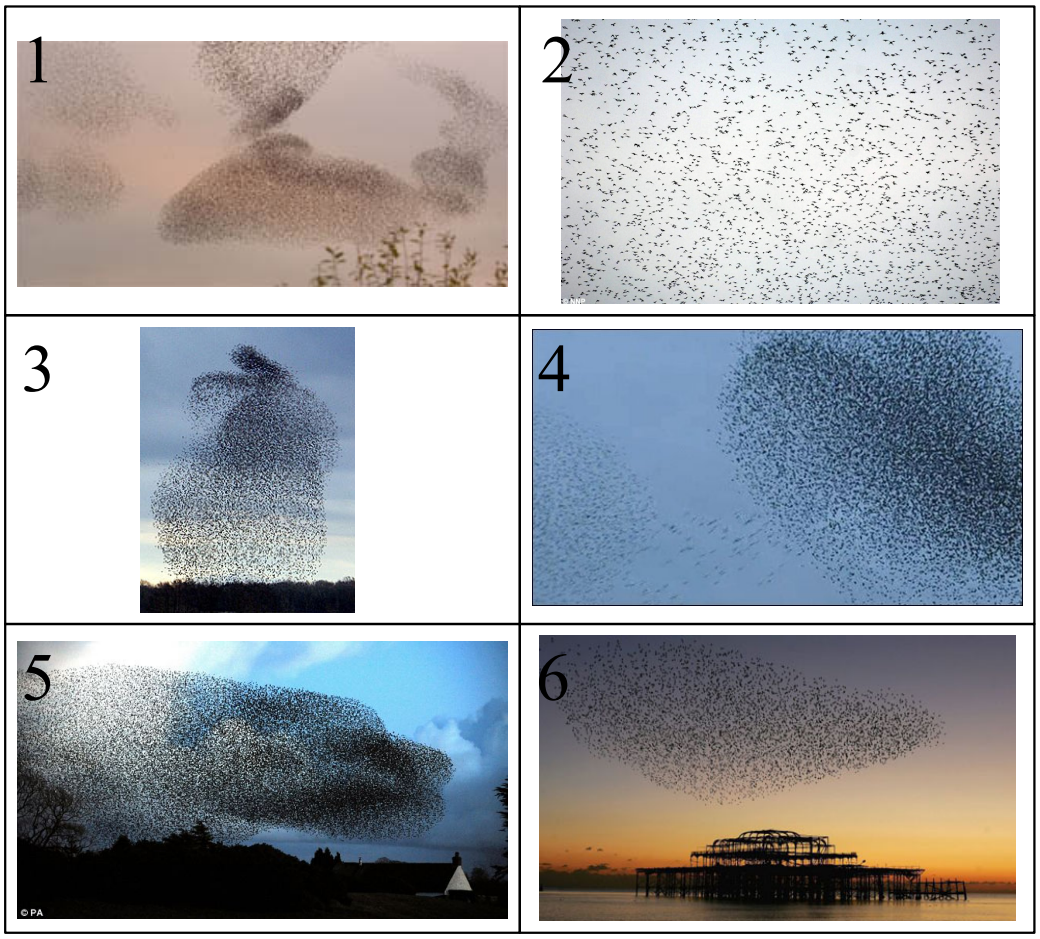

Figure 3:(SI) The images used to construct the corresponding first six the data points in Fig. 3e. These flocks were all found to be marginally opaque.

is then given by

$$\Theta' = \frac{g_{\max} - \bar{g}}{g_{\max} - g_{min}} = 1 - \frac{\bar{g} - g_{\min}}{g_{\max} - g_{min}} \tag{5}$$

This methodology is simple and has the advantage that it introduces no subjective bias into the image analysis. The error bars shown in Fig 3b,d,e are computed by using the greyscale levels g_- and g_+, respectively the pixel levels at the $\epsilon/2$ and $(100 - \epsilon/2)$ percentile of the pixel greyscale distribution, where here we choose $\epsilon = 5\%$. This was then used to compute the corresponding upper (Θ'_+) and lower (Θ'_-) bounds for our estimate of the opacity

$$\Theta'_- = \frac{g_+ - \bar{g}}{g_+ - g_{min}} \qquad \Theta'_+ = \frac{g_{\max} - \bar{g}}{g_{\max} - g_-} \tag{6}$$

This can be motivated by the heuristic argument that the most extreme 5% of pixels would be a reasonable alternative definition of sky/bird, mitigating the effects of any outlying pixels.

1.4 Camera Calibration

We calibrated our camera, and method of image analysis, by creating images of black disks randomly arranged on a white background with a known ratio of black to white pixels. This binary image is analogous to our images of birds against sky. This allows us to adjust the feature (circle) size in a controlled manner. By taking pictures of these images we can establish how accurately the camera is measuring the average greyscale, being the fraction of black pixels (bird) in the image, and hence the (flock) opacity. Importantly the disk (bird) sizes can be adjusted so that the size of these features falls below the pixel resolution of the camera, see Fig. S4. We find that the camera measures the opacity reasonably accurately, even when the feature size is below the single pixel resolution, as is often the case for the public domain images shown in Fig 3e.

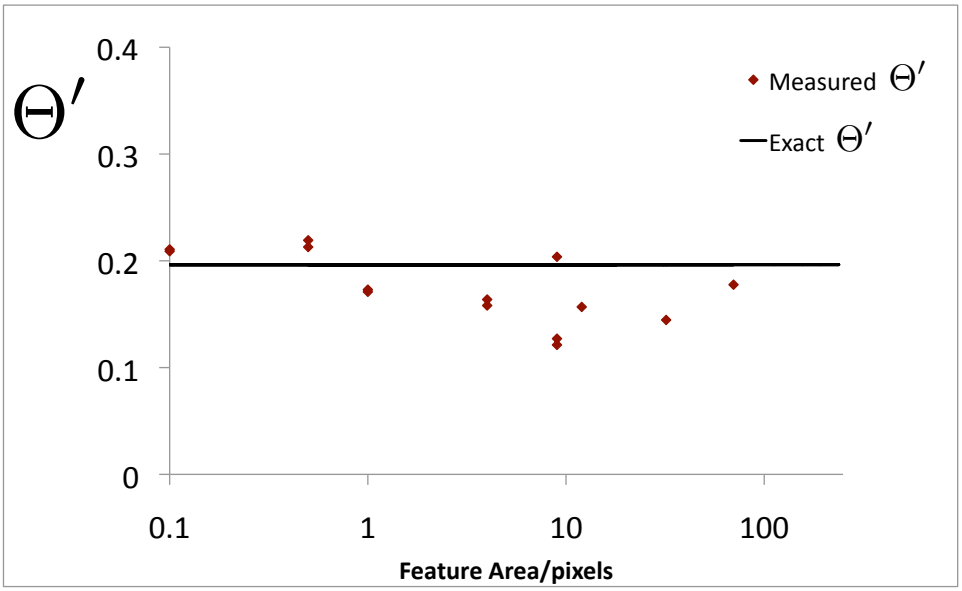

Figure 4: (SI) Opacities estimated from images consisting of black disks with different sizes. The opacity was estimated using Eq (S5 SI). The exact value of the opacity is shown as the solid black line.

1.5 Image Calibration

The images used in Fig 3e were collected from the public domain and had all been compressed using the jpeg compression algorithm. In order to assess the effect of this compression on the values of the opacity Θ' we ran our images of starling flocks through the jpeg compression algorithm, compressing them down to a size less than even the smallest file sizes in our public domain data set. By analysing the apparent opacity before and after compression we find that the measured opacity is largely unaffected by compression, see Fig. S5.

1.6 Cross Correlation

The acceleration of the centre of mass of the flock is used in constructing Fig 3c and is calculated by taking the coordinates of the centre of mass of the flock relative to a fixed point of reference, and lengthscale, within the image; in this case the tip of the old pier at Brighton. Each frame

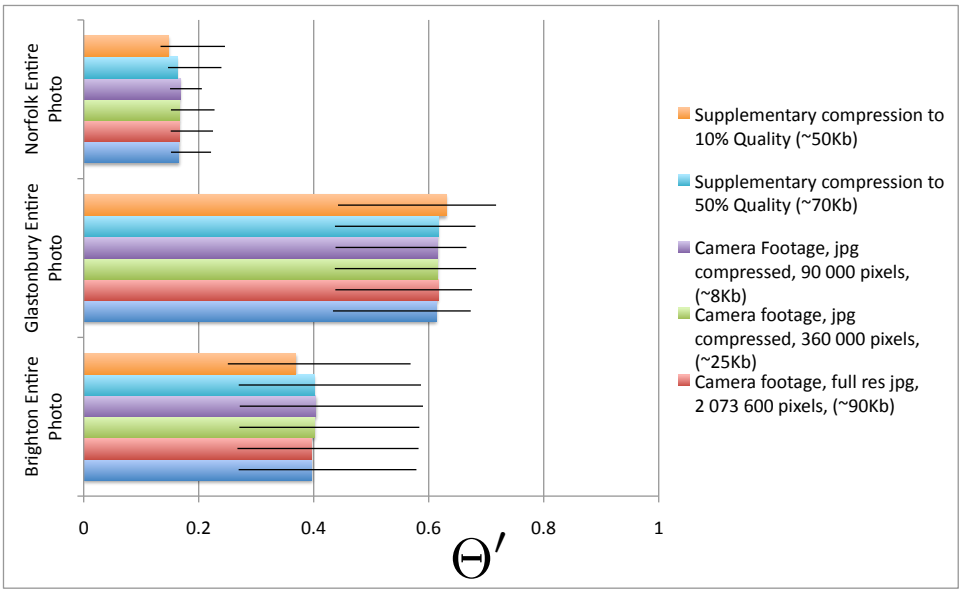

Figure 5: (SI) The differences in the calculated opacity after various levels of jpeg compression and size reduction. The error bars are calculated using Eq (S6).

yields a set of coordinates which, together with the known time step (inverse frame rate) is used to compute a scaled acceleration $a(t)$.

The cross correlation function between the acceleration relative to the mean $\delta a(t) = a(t) - \langle a \rangle$ and the opacity relative to the mean $\delta\Theta'(t) = \Theta'(t) - \langle \Theta' \rangle$ shown in Fig 3c is then

$$C(\delta t) = \frac{\langle \delta a(t) \delta\Theta'(t + \delta t) \rangle}{\sqrt{\langle \delta a^2 \rangle \langle \delta\Theta'^2 \rangle}} \tag{7}$$

Here a positive δt implies that the acceleration leads the opacity. This is as expected, as the flock needs first to move in order to change it's appearance, but it does show that a strong yet transitory signal indicating a change in direction is carried by the opacity of the flock.

The error bars in Fig 3c are the standard error in the estimate of the mean at each time point.

1.7 Defining the density

We define density as

$$\rho = N/(2\langle|\mathbf{r}_{ij}|^2\rangle) \tag{8}$$

where the average is over all pairs of individuals. This gives results which are qualitatively indistinguishable with those obtained by instead defining the density using the largest distance between any two individuals as the relevant swarm size.

The half time of the density autocorrelation function shown in Fig 2d is defined by

$$\frac{\langle\delta\rho(t)\delta\rho(t+\tau_\rho)\rangle}{\langle\delta\rho^2\rangle} = \frac{1}{2} \tag{9}$$

with $\delta\rho(t) = \rho(t) - \langle\rho\rangle$ and $\langle\delta\rho^2\rangle = \langle(\rho - \langle\rho\rangle)^2\rangle = \langle\rho^2\rangle - \langle\rho\rangle^2$.

2 Supplementary Results

2.1 Projection term leads to flock cohesion

In order to test how flock cohesion is controlled by the presence of the projection term we performed a number of simulations, first with a very small, but non-zero, projection term and then without it. The maximum distance between any two particles within a flock, R_{max} was recorded as a function of time, see Fig. S6. R_{max} gives a upper bound for the flock diameter, providing a useful metric to demonstrate the effectiveness of the projection term in producing bounded flocks; for an unbounded flock the maximum flock diameter will continually grow over time. Fig. S6 shows that the maximum linear size R_{max} of flocks grows without bound when $\phi_p = 0$. In this case the flock fragments into disconnected clusters that perform independent random walks, hence R_{max} continually increases (black traces). However, even a very small contribution from the projection term, here $\phi_p = 0.03$, is enough to prevent this from happening (red traces). This result is insensitive to the size of the flock and also to the precise choice of parameter values.

2.2 Anisotropic nearest neighbour distribution

The form of the nearest-neighbour distribution shown in Fig. S7 is in close agreement with a similar anisotropy observed in birds [2, 3] and fish [4, 5]. We believe that this is a consequence of the nature of the projection term, which makes it less likely for an individual to orientate itself toward its relatively large and dark (and hence edge-less) nearest neighbours.

2.3 Radial Density of nearest neighbours

The radial density in the immediate vicinity of an individual show a clear peak, see Fig. S8. This is very similar to observations of real animals [5, 6].

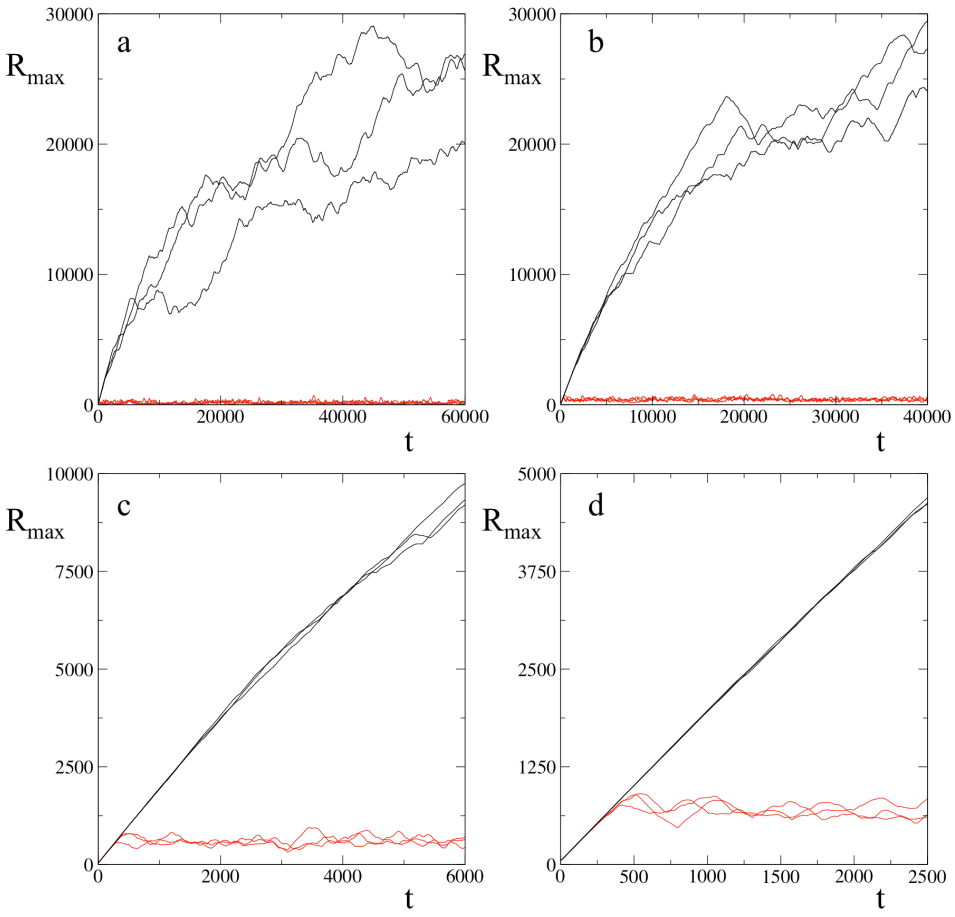

Figure 6: (SI) Maximum flock diameter for flocks containing (a) $N = 100$, (b) $N = 500$, (c) $N = 1000$ and (d) $N = 1500$ individuals generated by computer simulation of the hybrid projection model with $\phi_p = 0.03$, $\phi_a = 0.8$ and $\phi_n = 0.17$ (red), the same values as those used in Fig.2b in the main text, and in the absence of projection $\phi_p = 0.0$, $\phi_a = 0.83$ and $\phi_n = 0.17$ (black).

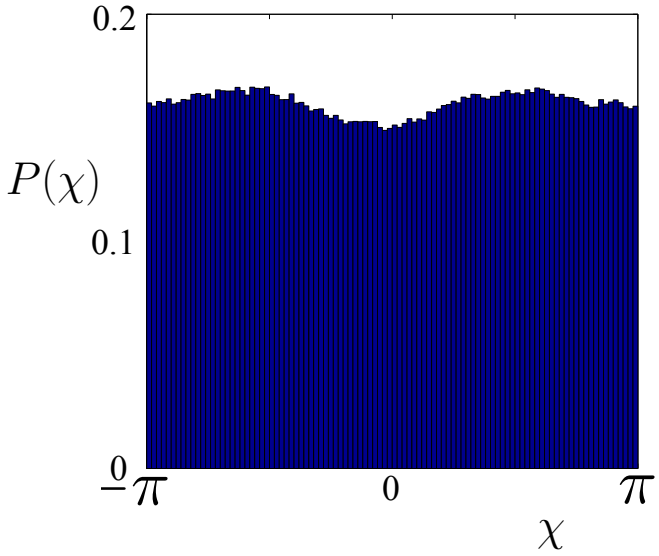

Figure 7: (SI) Probability density $P(\chi)$ for the angles (χ) between the velocity of (all) of the i^{th} individuals, parallel to $\mathbf{v}_i$, and the vector $\mathbf{r}_{ik}$ to each of its 4 nearest neighbours, labelled by the index k, as in the text. The peaks at $\chi = \pm\pi/2$ indicates that nearest neighbours are preferentially orientated to the sides of the individuals, rather than in front or behind. These results were gathered for a swarm of $N = 100$ isotropic individuals over 10,000 time steps with $\phi_a = 0.85$, $\phi_p = 0.05$.

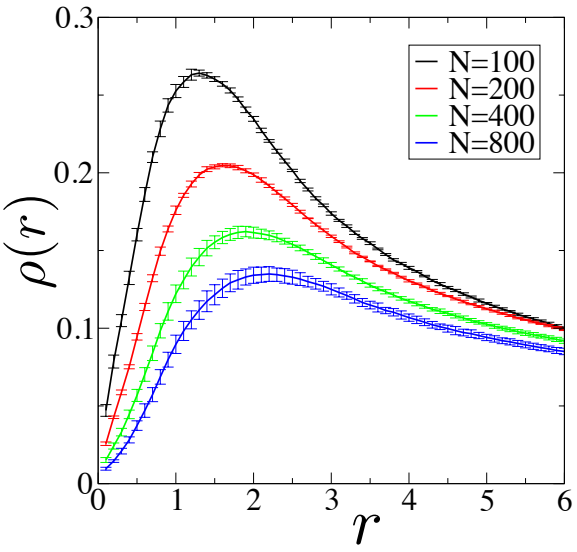

Figure 8: (SI) Average radial density of neighbouring birds relative to an individual (at $r = 0$) for $\phi_a = 0.85$ and $\phi_p = 0.05$. The density is per unit area, in units where the size of each isotropic individual is unity.

2.4 Effects of steric interactions

We can also introduce a short range repulsion/steric interaction to the model. Whenever the distance between two individuals drops below a threshold they then have a new behavioural update rule in which they simply move away from neighbours so as to avoid collisions. Such a steric interaction has little effect on the behaviour of the model at the qualitative level. This is because the projection term already acts to prevents the flocks becoming too dense due to the fact that it steers individuals away from opaque (dense) directions. In order to investigate the effects of this we introduce a steric interaction term in which birds fly away from their nearest neighbours if they get within two length units. The order parameter, α, linear flock length, R_{max}, and opacity, θ, for such a flock change little and are shown in Fig. S9.

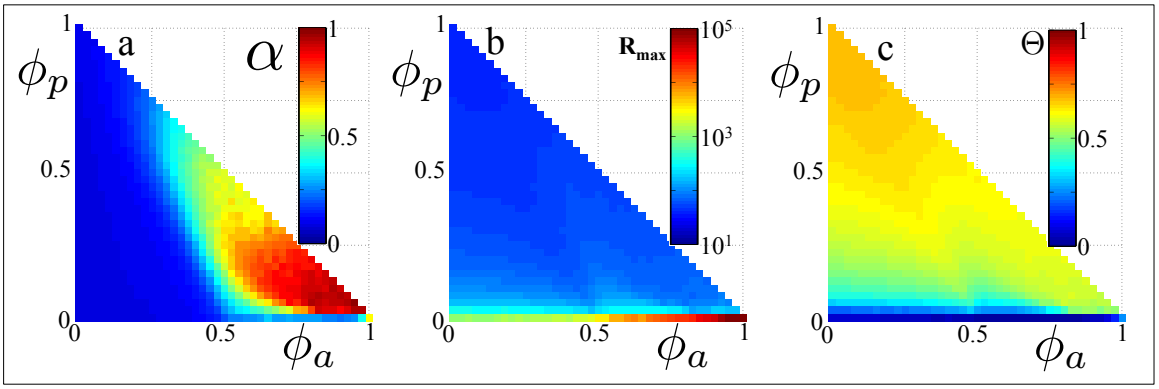

Figure 9: (SI) a) The order parameter, α, b) linear flock length, R_{max}, and c) opacity, θ, as a function of the parameters ϕ_p and ϕ_a for a flock of 100 isotropic individuals which repel each other when within 2 length units. Each small colored square (point), corresponding to a pair of parameter values $\{\phi_a, \phi_p\}$, is an average value over 400,000 timesteps for $N = 100$ individuals.

2.5 Effects of anisotropic vision for individuals.

Birds and other flocking animals do not have fully isotropic vision, e.g. birds cannot see what is directly behind them. In order to study how this might affect the behaviour of the model and the emergence of marginal opacity we introduce a blind angle (γ) behind each individual, outlined in Fig. 10. We first define 'behind' as the opposite direction to the velocity (hence $(arg(\underline{v}_i) + \pi)$ for individual i). Any boundary falling within the angular region $(arg(\underline{v}_i) + \pi) \pm \gamma/2$ (shaded in blue on Fig. 10) will not contribute to the projection term.

For values of $\gamma < 4\pi/5$, well in excess of what is realistic, marginal opacity emerges robustly and flock cohesion is unaffected. This is shown by the values for opacity (θ) and swarm size (R_{max}) in Fig. 11, where the standard deviations in these values can be seen to be relatively small. As γ becomes unphysically large ($\gamma > 4\pi/5$) the swarm opacity and density are more substantially affected. While the flock now remains strictly cohesive it becomes possible for (groups of) individuals to transiently move directly away from the bulk of the flock only rejoining it when they have rotated sufficiently to pick up the flock again. This rotation can

be slow if there are a substantial number of individuals in any such breakaway group. When this is the case, the maximum separation between two individuals in the swarm becomes a poor measure of the local density, as it is sensitive to outliers that have transiently lost contact with the remainder of the swarm, hence we also show the variation of the average nearest neighbour distance R_{min} in Fig. 11.

In fact it is probably more physically realistic that the bird ignores *all* sensory input coming from within the blind angle, i.e. excluding also the co-alignment term. In this case we obtain slightly more dense flocks that are able to remain cohesive and marginally opaque for a greater range of γ, see Fig. 12.

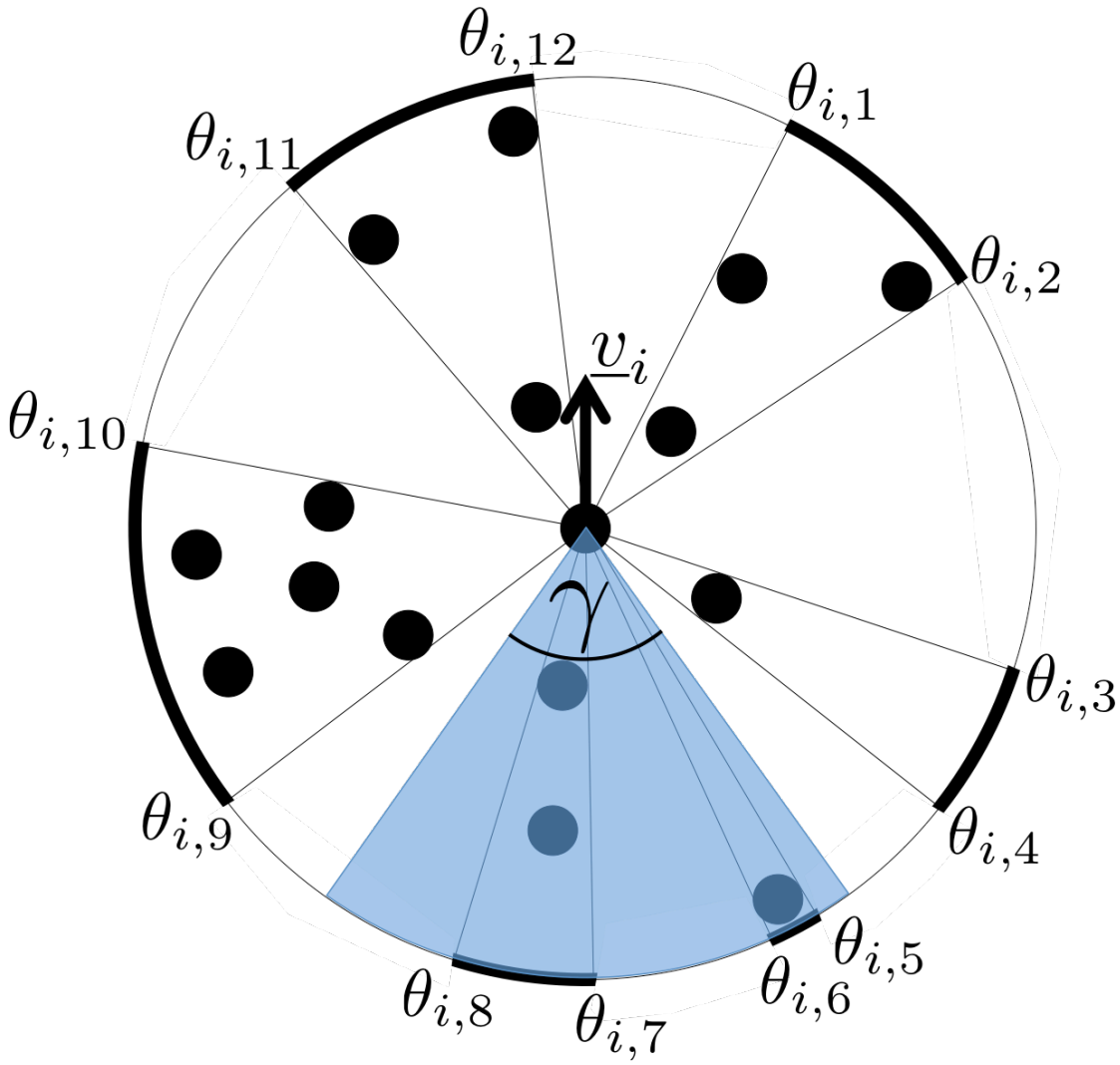

Figure 10: (SI) Diagram detailing the how the bind angle (γ) corresponds to the angular region directly behind an individual (here i with velocity $\underline{v}_i$) over which the boundaries do not contribute to the projection term (shaded area). In this example the projection term given by Eq. 1(main text) would not include $\theta_{i,5-8}$

.

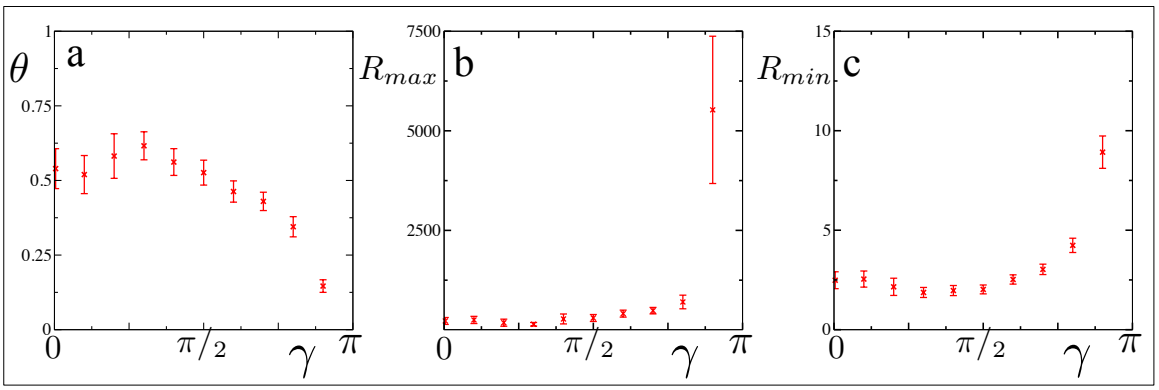

Figure 11: (SI) a) Opacity (θ), b) swarm size (R_{max}) and c) average nearest neighbour distance (R_{min}) for swarms of $N = 100$ individuals with varying blind angles (γ) within which individuals do not contribute to the projection term in Eq [3](main text). The model parameters are $\phi_a = 0.8$ and $\phi_p = 0.03$, to match those used in Fig. 2b(main text). Results show the mean and standard deviation over 50,000 time steps following a 6000 time step equilibration period.

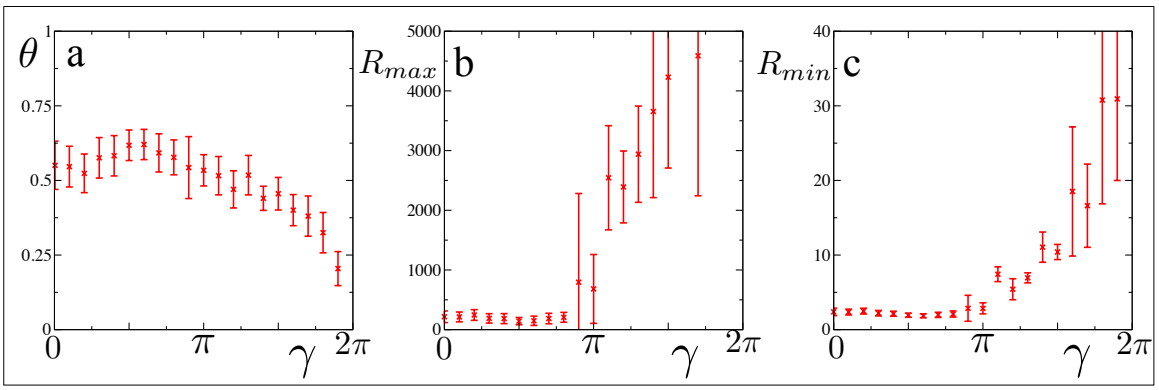

Figure 12: (SI) a) Opacity (θ), b) swarm size (R_{max}) and c) average nearest neighbour distance (R_{min}) for swarms of $N = 100$ individuals with varying blind angles (γ) within which contributions to *both* the projection term and co-alignment term are ignored. The model parameters are $\phi_a = 0.8$ and $\phi_p = 0.03$, to match those used in Fig. 2b(main text). Results show the mean and standard deviation over 50,000 time steps following a 6000 time step equilibration period.

3 Comparison with metric based models

In order to highlight some of the advantages of a global, metric free model, we compared it to a standard local, metric based model for flocking. The choice of model is somewhat arbitrary; any local repulsion/orientation/attraction model could have been chosen. Because of this we chose to make a simplest case model that includes the core of many established metric models capable of creating coherent flocks [7, 8].

We chose a model in which each particle has three interaction radii, a repulsion from all particles at a distance $r < r_r$, co-alignment with all particles in the region $r_r < r < r_o$, and attraction to all particles in the region $r_o < r < r_a$. Each particle moves with a constant velocity, $v = 1$, and updates its direction and position every timestep, which have length $dt = 0.1$. Our simulation of this model was coded in C++ and employed simulation parameters $r_r = 1$, $r_o = 10$ and $r_a = 15$ for the repulsion, orientation and attraction ranges respectively, shown as the red ($N = 300$) and black ($N = 100$) traces in Figs. S14, S15 and all traces in Fig. S13. Where it was necessary to modify these parameters the green trace on Figs. S14, S15 corresponds to $N = 300$, $r_r = 1$, $r_o = 17$ and $r_a = 26$. The results from this simple attraction-repulsion model are compared with our hybrid projection model in Figs. S13, S14, S15. In order to define an opacity in Fig. S15 the individuals size must be defined. We take this as 0.25 in the same units. This value is chosen because the STARFLAG data shows the nearest neighbor spacing is often around 1m, and the length of a starling is around 0.25m [9]. So there is a factor of 4 between the two units. The dashed lines in Fig. S14b are the diameter of the orientation zone $2r_o$, which it is appropriate to compare with R_{max}, the maximum distance across the flock. This, along with the change in units leads to a factor of 8 scaling from $r_o = 10$ and $r_o = 17$, respectively, to the value given in Fig. S14b in bird length units.

Although this is an arbitrary choice of model in order to test out hypothesis against, the

results will be the same (within a scaling factor) for any model that similarly defines metric interaction radii.

3.1 Global Interactions result in more robust flocks

Models that include only local interactions produce flocks that can fragment or disperse if the simulation parameters and initial conditions are not carefully chosen. If an agent has a limited, metric-based interaction radius the simulation parameters (such as length of timestep, noise, speed, range(s) etc.) must be selected to prevent moves that could leave an individual disconnected from the flock, i.e. with no other particles within its interaction radius. If this were to happen there would be no mechanism to ensure that it rejoins the flock. Such fragmentation is always a danger when the flock is perturbed, for example by predation, so as to result in a (group of) individual(s) being separated from the flock. It also fails to capture how a flock might form from an initially disperse state. This is characterized in Fig. S13, where flocks following the hybrid projection model are shown to recover from an arbitrary perturbation involving a 16X metric expansion of the flock while local, metric based flocks fail to aggregate. The recovery of the hybrid projection model is independent of the parameters used, provided only that $\phi_p > 0$. In contrast, local metric based models are unable to reliably recover from perturbations that move any (groups of) individual(s) outside the attraction radius.

This effect is also highlighted in supplementary movies S3, and S4, in which swarms of individuals are introduced to a simple predator (The predator travels at a speed of $2 * v_0$ and is attracted to the centre of mass of the swarm. The individuals react to the predator when it is within $10 * dt * v_0$ and their response is to travel directly away from it at $1.5 * v_0$). In Supp.Mov. S3, the predator is unable to separate a swarm of individuals following the hybrid projection model ($\phi_p = 0.2$, $\phi_a = 0.7$), the global nature of the interactions between individuals meaning it is always able to reform. In Supp.Mov. S4, individuals have a limited interaction

radius. In this case they don't respond to other members of the swarm that are separated by more than $30 * v_0 * dt$. The difference in the ability of the swarm to remain as one cohesive group is clear from the two movies.

3.2 Metric free interactions scale with the flock size

As reported by [9], the interactions within bird flocks are now understood to be scale free, scaling with the overall extent of the flock. This would seem to be reflected in the failure of metric based models to cope with increasing N unless the behavioral parameters are themselves continually adjusted, see e.g. Fig. S14. This is because the metric-based nature of these models effectively fixes the density, through the inter-particle spacing, see Fig. S15b. As N increases any fixed interaction range will eventually encompass only a small fraction of the flock, leading to a breakdown in transfer of alignment information and loss of global alignment α, see Fig. S14a The only way to adjust the model to obtain realistic behavior is to change the interaction radii accordingly, so that they once again encompass a significant proportion of the flock; essentially the model is demanding global interactions. This necessarily leads to a rather complex (highly parameterized) model in which individuals make decisions based on the position and orientation of an ever increasing number of neighbors; for a flock with $N = 300$ each individual responds to the positions and velocities of ~ 270 of its neighbors, as shown in Fig. S14c. Many of these are obscured from its view, as discussed in the next section.

3.3 Metric based interaction ranges lead to fixed density and opaque flocks

The hybrid projection model results in flocks that are marginally opaque, that is to say that visual information can often pass, uninterrupted, across the entire flock. This seems to be supported by observations. Any model that fixes density, i.e. through a fixed nearest neighbor distance, must eventually give rise to fully opaque flocks as more individuals are added (see

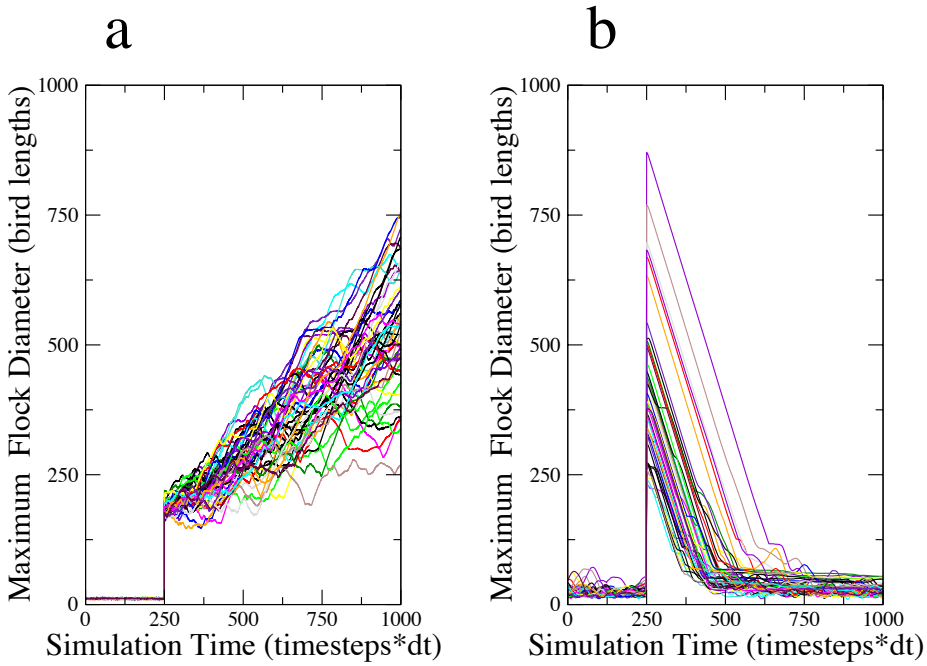

Figure 13: (SI) Maximum flock diameter for 50 different simulations (each trace) of a flock of $N = 50$ individuals created using a) Local and b) Hybrid Projection Models following a 16X linear expansion in two dimensions. We used typical parameters for a flock of $N = 100$ birds outlined above and a hybrid projection model with $\phi_p = 0.2$, $\phi_a = 0.7$ and $\phi_n = 0.1$. Technical detail: the dimensionless time corresponding to each time step was $dt = 0.1$ in the metric model and $dt = 1$ in the hybrid projection model and so we have scaled the simulation time steps by this factor to obtain a fair comparison of the relative diameters, which would otherwise be different (scaled) by a factor of 10.

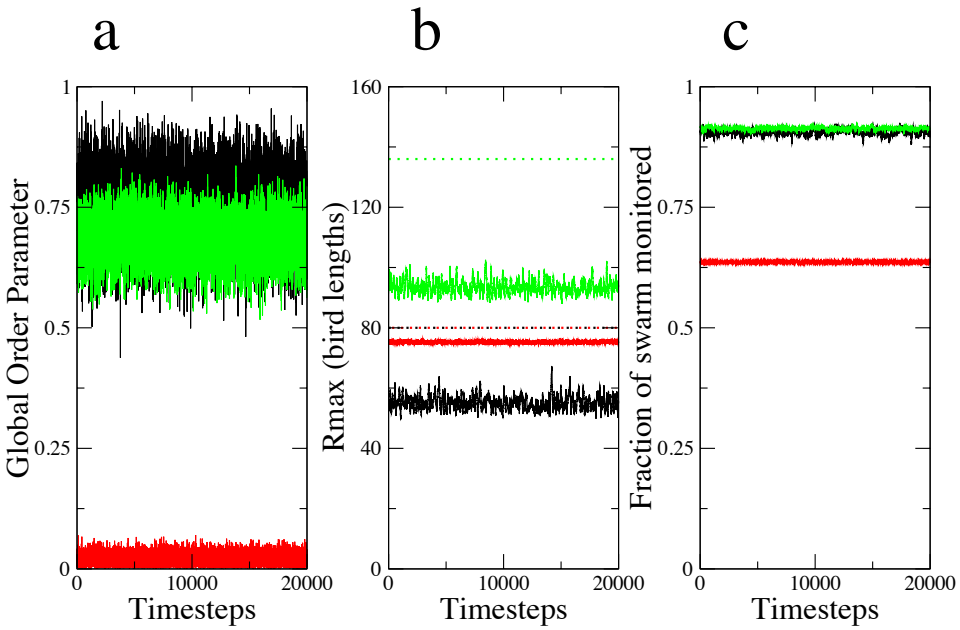

Figure 14: (SI) Breakdown of a local model. (a) As the number of individuals in the flock is increased from $N = 100$ (black) to $N = 300$ (red) the global order parameter, α, falls to near zero, unless the interaction ranges are extended to the larger values given in the text (green). (b) The alignment interaction diameter (range) in bird length units (dashed line, see text for details) is significantly higher than the maximum extent of the flock (R_{max}) for realistic flocks (black, green) and therefore encompasses almost the entire flock. (c) The increased interaction ranges result in an individual monitoring the position and velocity of about 90% of its neighbors (they giving input to the model for that individuals behavior) for $N = 300$ (green), as was the case for $N = 100$ (black).

mean field scaling analysis in main text). In the worst case scenario this could result in behavior dominated by fictitious phantom interactions between individuals that are completely occluded from one-another. Fig. S15a shows that local metric based flocks are almost entirely opaque. This is due to the fact that the individuals essentially form a close packed liquid-like phase with little change in the nearest neighbor separation; see Fig. S15b. This results in a large fraction of unphysical phantom interactions, depending on whether one imagines that some (Fig. S15c) or all (Fig. S15d) of a neighboring individual must be seen for a realistic interaction to occur. Also, due to the metric nature of the interaction radii, as the flock gets bigger the information transfer across the length of the flock becomes far less efficient as the interaction radii becomes smaller relative to the extent of the flock. This means that a change in parameters is needed to prevent the flock from entering a solid like state, in which global order is lost.

4 Phenotypical Behaviour under the Hybrid Projection Model

Fig. S16 shows a number of "phenotypes" supported by the hybrid projection model. In this figure the point in parameter space denoted I involves swarms with low global order α and weakly correlated internal dynamics, somewhat reminiscent of a swarm of flying insects. The point F can exhibit circulating vortex-like swarms, somewhat reminiscent of those observed in shoals of fish [10]. This morphology doesn't appear in swarms of isotropic individuals but is seen in these anisotropic individuals that mimic the long-and-thin shape of fish. The point B has a relatively high global order α and is similar to many of the swarms seen for isotropic individuals. It is perhaps more reminiscent of travelling flocks of birds. In each case a corresponding snapshot of a typical swarm configuration is shown. These results lead us to speculate that this model may provide a method to classify swarming behaviour across species, e.g. according to the values of ϕ_p, ϕ_a and σ (see Supp.Movs. S5-S7). As discussed below intermediate regions exist in which the entire swarm can switch spontaneously between two distinct behavioural modes,

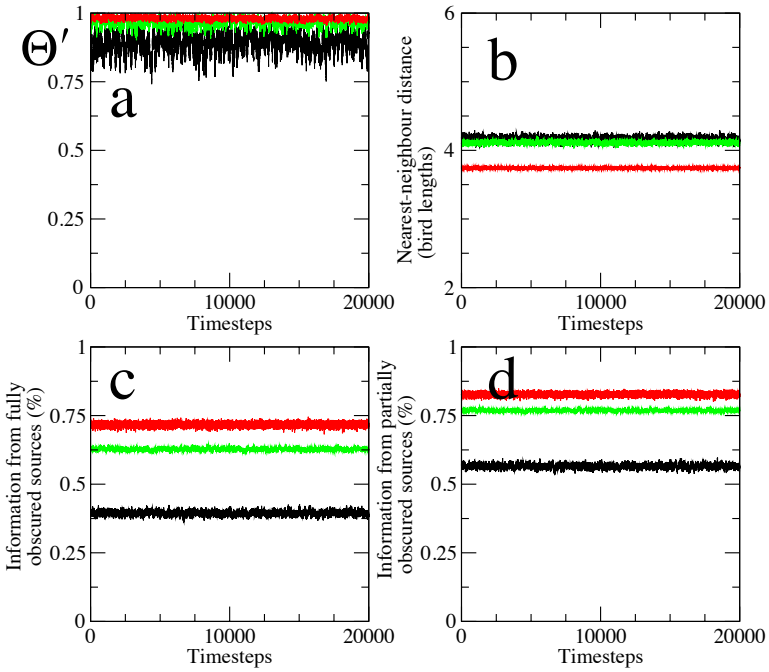

Figure 15:(SI) Unphysical nature of a local model with the same parameters as used in Fig. S14. (a) Flocks remain fully opaque in time from the point of view from an external observer. (b) This is due to the metric nature of the model that fixes the average separation between individuals in time. (c,d) The proportion of neighbors interacting with an individual through this model that are (c) completely and (d) partly occluded from its view remains high throughout.

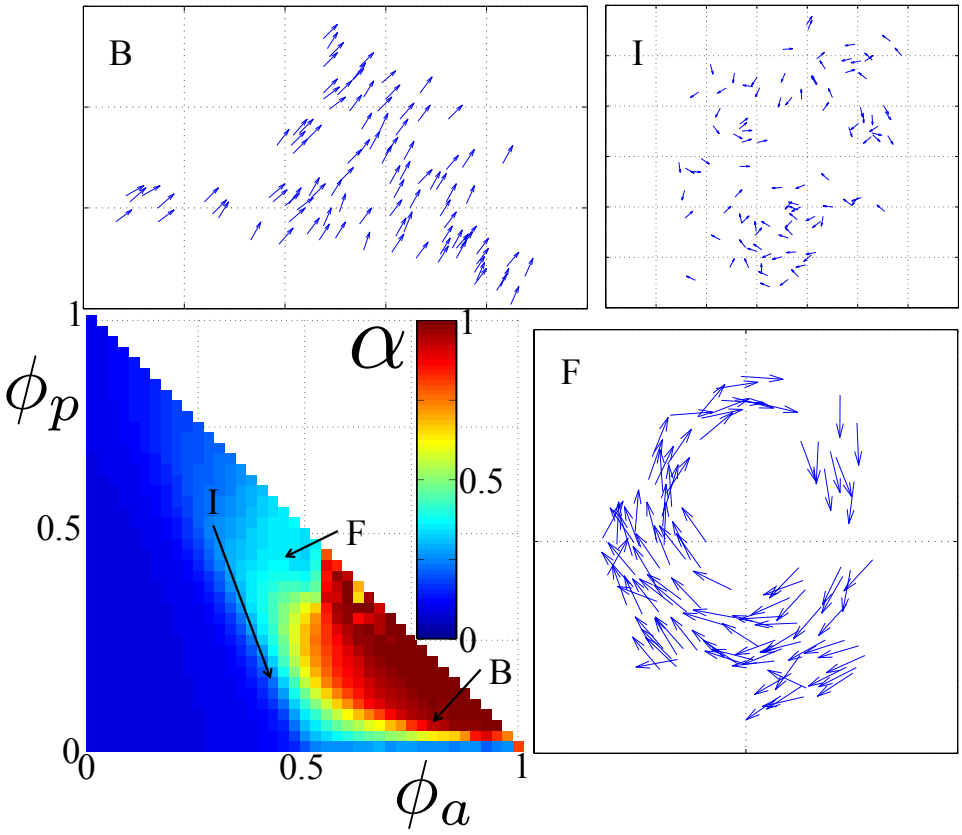

Figure 16: (SI) Shown in the bottom left is the variation of the global order parameter α for a swarm of 100 anisotropic individuals (10:1 long-and-thin) with the relative weights of the projection ϕ_p and alignment ϕ_a terms (compare with Fig 2e for isotropic individuals). Shown in the other panels are snapshots of the trajectories at each of the corresponding points indicated on the phase plane. Points B, F and I correspond to Supp. Movs. S5, S6, and S7, respectively.

reminiscent of the ability of real animals to change their behaviour in response to a threat.

4.1 Vorticity of the flock, milling in fish

The vorticity ω of a swarm is here defined as the average tangential component of the velocities with respect to the centre of mass of the swarm according to

$$\omega = \frac{1}{N}\sum_{i=1}^{N} \frac{\delta \mathbf{r}_i}{|\delta \mathbf{r}_i|} \times \frac{\mathbf{v}_i}{|\mathbf{v}_i|} \tag{10}$$

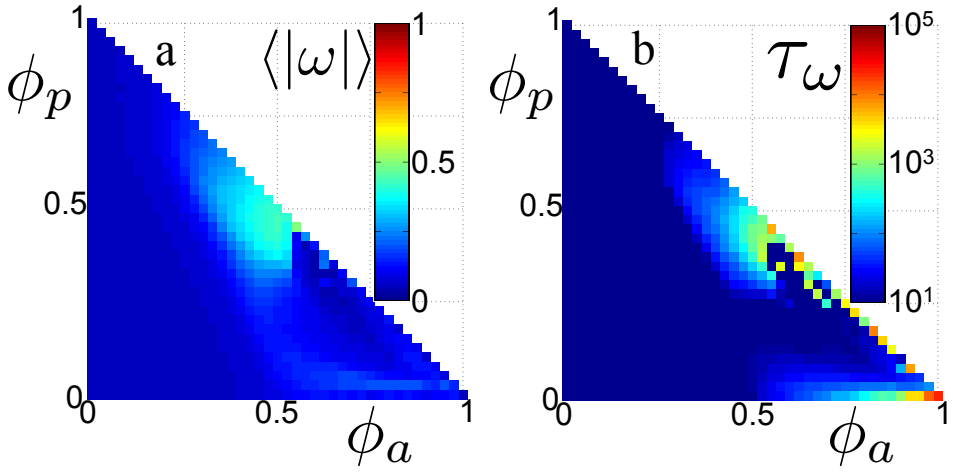

Figure 17: (SI) (a) The variation of the time averaged magnitude of the vorticity, $\langle|\omega|\rangle$, and (b) the vorticity correlation time τ_ω in simulation time-steps with the relative weights of the projection ϕ_p and alignment ϕ_a terms. Following the main text all swarms contain $N = 100$ isotropic individuals and each point is an average of 3 simulations over 100,000 time-steps following a 25,000 time-step pre-equilibration period.

with $\delta\mathbf{r}_i = \mathbf{r}_i - \bar{\mathbf{r}}$ and $\bar{\mathbf{r}} = \frac{1}{N}\sum_{i=1}^{N}\mathbf{r}_i$ the centre of mass of the flock. The vorticity satisfies $-1 < \omega < 1$ with $\omega > 0$ for anticlockwise circulation and $\omega < 0$ for clockwise motion. The vorticity autocorrelation time τ_ω is defined by

$$\frac{\langle\omega(t)\omega(t+\tau_\omega)\rangle}{\langle\omega^2\rangle} = \frac{1}{2} \tag{11}$$

Fig. S17 shows results obtained for swarms of anisotropic individuals; isotropic individuals tend not to exhibit such high vorticity.

Fig. S17a clearly shows a region of increased vorticity in a region corresponding to one of reduced order (centre of mass velocity) α in Fig. S16. As can be seen from Fig. S17b vorticity decorrelation is observed on computationally accessible timescales. What is the mechanism for this loss of correlation? The trajectory shown in Fig. S18 shows that this can arise due to the ability of the swarm to switch between clockwise rotation, anticlockwise rotation and translating phases. The time τ_ω can roughly be associated with the time between switching

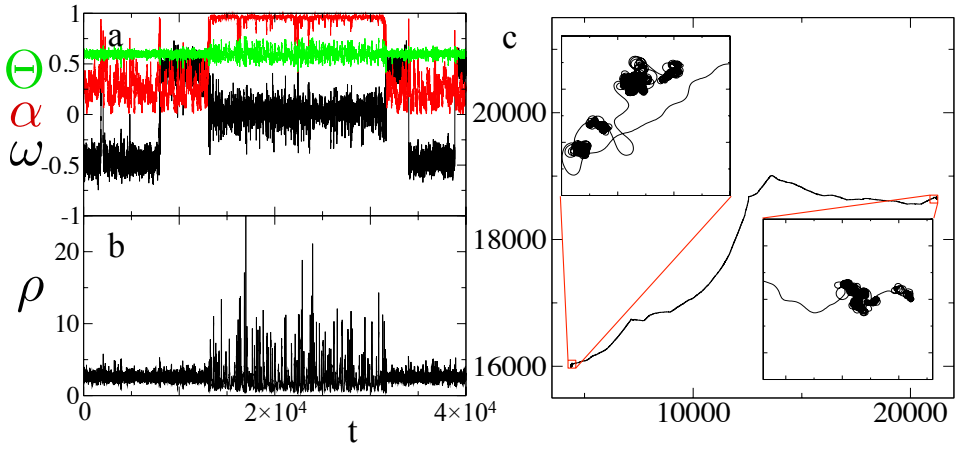

Figure 18: (SI) The behaviour of a swarm of $N = 100$, 10:1 anisotropic individuals with $\phi_p = 0.4$, $\phi_a = 0.525$. Shown is (a) The time variation of the opacity Θ (green), order α (red) and vorticity ω (black) against dimensionless time t, measured in units of the simulation timestep. (b) The time variation of the density ρ, measured in dimensionless units of the inverse squared length of each individual, over the same period. (c) The trajectory of the centre-of-mass of the swarm over a much longer period; inset we zoom in on the apparent kinks in the trajectory, revealing repeated switching between circulating and translating phases, somewhat reminiscent of the run-and-tumble motion of bacteria [11]. The period shown in (a) and (b) corresponds to the first section of the trace shown in (c). The axes show the dimensionless cartesian position, divided by the length of each individual.

events. Significantly, switching occurs with very little change in opacity or average density, although there is an increase in the amplitude of fluctuations about these average values when the swarm enters the translating phase. This is further evidence of the robust nature of the emergence of marginal opacity within our model.

4.2 Extreme regions of the parameter space

We already know that the model produces unphysical behaviour for extreme values of the parameters, e.g. it disperses if $\phi_p = 0$. For strong alignment (ϕ_a) and very low noise (ϕ_n), i.e. near the bottom of the diagonal boundary of the phase planes such as shown in Fig 2e or S16, the swarm can adopt a single file arrangement that would also appear to be unphysical. This seems

to be stable, or at least extremely long-lived and is associated with the fact that we have (precisely) fixed the velocity of all individuals. In the, rather unphysical, case that there is almost no noise the swarm is unable to escape from this state because the projection term is parallel to the velocity at all times, and so it has little effect.

For very low alignment (ϕ_a) and noise (ϕ_n), i.e. in the top left corner of Fig 2e or S16, the swarm can adopt a stable, linear conformation in which the swarm condenses to a high density state, with little global order (small α). Morphologies consisting of a single line, or three-pronged rotationally symmetric structures seem to be stable in this case. Again, these are rather unphysical. In this case the projection term causes most individuals to reverse direction at each time-step. These morphologies are long-lived, leading to the long density auto correlation times observed in this region in Fig 2f. This behaviour is largely attributed to our discrete time approach combined with the lack of any momentum (or memory) between time steps.

5 Movie Captions

Ten movies are available to give examples of the type of data on real starling flocks used in this study and the qualitative behaviour of swarms generated by the hybrid projection model.

Full resolution versions of these movies are available for download at:

https://files.warwick.ac.uk/djgpearce/browse/PNAS+SI+Movies

5.1 Supp.Movs. S1, S2

Supp.Movs. S1 & S2, are of the starling flocks shown in the red and black traces of Fig. 3b, respectively. These were taken at Brighton, East Sussex, UK on 14/11/2011 between 15:30 and 16:30. These are typical of the type of footage captured of Starling flocks.

5.2 Supp.Movs. S3, S4

Supp.Mov. S3 shows the robustness of the hybrid projection model under attack by a simple predator trying to split up the swarm. Due to the global nature of the interactions between individuals, the flock is always able to reform after the predator's attacks.

Supp.Mov. S4 shows how a swarm responds to the same predator when the interactions between individuals have a limited range. This means it becomes possible for the predator to completely sever interaction between two regions of the swarm resulting in a far less cohesive swarm that cannot guarantee that it will reform after becoming scattered.

Both Supp.Mov. S3 & S4 feature $N = 100$ individuals with $\phi_p = 0.2$, $\phi_a = 0.7$. The predator travels at a speed of $v_p = 2 * v_0$ and is attracted to the centre of mass of the swarm. The individuals react to the predator when it is within $r_p = 10 * dt * v_0$ and their response is to travel directly away from it at $v_{response} = 1.5 * v_0$. In Supp.Mov. S4, individuals only react to other members of the swarm within $r_{limit} = 30 * dt * v_0$.

5.3 Supp.Movs. S5, S6, S7

Movies S5, S6 & S7, show the behaviour of a swarm of $N = 100$, 10:1 anisotropic (long and thin) individuals within our hybrid projection model. These movies show the distinct behavioural phenotypes observed with a change in the parameters ϕ_p and ϕ_a, highlighted in Fig. S16. Each frame is a single time step.

Supp.Mov. S5, are obtained for $\phi_p = 0.1$, $\phi_a = 0.75$, point B in Fig. S16; this shows a phenotype displaying a high level of orientational order similar to that seen in migratory animals.

Supp.Mov. S6, are obtained for $\phi_p = 0.45$, $\phi_a = 0.45$, point F in Fig. S16; this shows a phenotype displaying a high swarm vorticity much like the milling behaviour observed in fish.

Supp.Mov. S7, are obtained for $\phi_p = 0.175$, $\phi_a = 0.45$, point I in Fig. S16; this shows

a phenotype with lower order in which there is a higher variation in the density of the swarm reminiscent of the swarming behaviour observed in insects.

5.4 Supp.Movs. S8, S9, S10

Supp.Movs. S8, S9 & S10 show the qualitative effects of the introduction of a "blind angle" behind each individual. This means that the projection term does not respond in any way to individuals within a $\pi/8$ cone directly behind them. Supp.Movs. S8, S9 & S10, show simulations with exactly the same parameters as movies S5, S6 & S7, respectively, and highlight the modest effect of the blind angle on the behaviour.

References and Notes

[1] Couzin I, Krause J, James R, Ruxton G, Franks N (2002) Collective memory and spatial sorting in animal groups. *J. Theor. Biol.* 218:1–11.

[2] Ballerini M, et al. (2008) Interaction ruling animal collective behavior depends on topological rather than metric distance: evidence from a field study. *Proc. of Nat. Acad. Sci.* 105:1232–1237.

[3] Ballerini M, et al. (2008) Empirical investigation of starling flocks: a benchmark study in collective animal behavior. *Animal Behaviour* 76:201–215.

[4] Partridge B, Pitcher T, Cullen J, Wilson J (1980) The three-dimensional structure of fish schools. *Behav. Ecol. Sociobiol.* 6:277–288.

[5] Partridge B, Johansson J, Kalish J (1983) The structure of schools of giant bluefin tuna in cape cod bay. *Environ. Biol. of Fish e* 9:253–262.

[6] Lukeman R, Li Y, Edelstein-Keshet L (2010) Inferring individual rules from collective behavior. *Proc. of Nat. Acad. Sci.* 107:12576–12580.

[7] Schellinck J, White T (2011) A review of attraction and repulsion moels of aggregation: Methods, findings and a discussion of model validation. *Ecol. Modell.* 222:1897–1911.

[8] Giardina I (2008) Collective behavior in animal groups: theoretical models and empirical studies. *H.F.S.P. Journal* 2:205–219.

[9] Cavagna A, et al. (2010) Scale-free correlations in starling flocks. *Proc. of Nat. Acad. Sci.* 107:11865–11870.

[10] Parrish J, Edelstein-Keshet L (1999) Complexity, pattern, and evolutionary trade-offs in animal aggregation. *Science* 284:99–101.

[11] Berg. H (2004) *E.Coli in Motion.* (Springer).